

Steady X-Ray Synchrotron Emission in the Northeastern Limb of SN 1006

Satoru Katsuda¹, Robert Petre¹, Koji Mori², Stephen P. Reynolds³, Knox S. Long⁴, P. Frank Winkler⁵, and Hiroshi Tsunemi⁶

Satoru.Katsuda@nasa.gov, Robert.Petre-1@nasa.gov,
mori@astro.miyazaki-u.ac.jp, reynolds@ncsu.edu, long@stsci.edu,
winkler@middlebury.edu, tsunemi@ess.sci.osaka-u.ac.jp

ABSTRACT

We investigate time variations and detailed spatial structures of X-ray synchrotron emission in the northeastern limb of SN 1006, using two *Chandra* observations taken in 2000 and 2008. We extract spectra from a number of small ($\sim 10''$) regions. After taking account of proper motion and isolating the synchrotron from the thermal emission, we study time variations in the synchrotron emission in the small regions. We find that there are no regions showing strong flux variations. Our analysis shows an apparent flux decline in the overall synchrotron flux of $\sim 4\%$ at high energies, but we suspect that this is mostly a calibration effect, and that flux is actually constant to $\sim 1\%$. This is much less than the variation found in other remnants where it was used to infer magnetic-field strengths up to 1 mG. We attribute the lack of variability to the smoothness of the synchrotron morphology, in contrast to the small-scale knots found to be variable in other remnants. The smoothness is to be expected for a Type Ia remnant encountering uniform material. Finally we find a spatial correlation between the flux and the cut-off frequency in synchrotron emission. The simplest interpretation is that the cut-off frequency depends on the magnetic-field

¹NASA Goddard Space Flight Center, Greenbelt, MD 20771, U.S.A.

²Department of Applied Physics, Faculty of Engineering, University of Miyazaki, 1-1 Gakuen Kibana-dai Nishi, Miyazaki, 889-2192, Japan

³Physics Department, North Carolina State University, Raleigh, North Carolina 27695

⁴Space Telescope Science Institute, 3700 San Martin Dr., Baltimore, MD 21218, U.S.A.

⁵Department of Physics, Middlebury College, Middlebury, VT 05753

⁶Department of Earth and Space Science, Graduate School of Science, Osaka University, 1-1 Machikaneyama, Toyonaka, Osaka, 560-0043, Japan

strength. This would require that the maximum energy of accelerated electrons is not limited by synchrotron losses, but by some other effect. Alternatively, the rate of particle injection and acceleration may vary due to some effect not yet accounted for, such as a dependence on shock obliquity.

Subject headings: acceleration of particles — ISM: individual objects (SN 1006)
— ISM: supernova remnants — shock waves — X-rays: ISM

1. Introduction

SN 1006 is the supernova remnant (SNR) for which X-ray synchrotron emission from diffusive shock accelerated electrons was first proposed (Reynolds & Chevalier 1981) and detected in X-rays with *ASCA* (Koyama et al. 1995). It remains an unrivaled laboratory for studying these phenomena because of its large size ($\sim 30'$ diameter; Winkler & Long 1997) and low interstellar absorption ($6.8 \times 10^{20} \text{ cm}^{-2}$; Dubner et al. 2002). Very recently, the HESS team reported the firm detection of TeV γ -ray emission from this SNR (Acero et al. 2010).

One of *Chandra*'s great discoveries in particle acceleration physics was that rims of SN 1006 and other young SNRs are very narrow, much narrower than the $1/12$ shock radii expected for a strong shock with a compression ratio of 4 (e.g., Long et al. 2003; Bamba et al. 2003; 2005). There is a general consensus that these narrow filaments are indirect evidence for strongly amplified magnetic fields at or upstream of the shock. However, the origin of the narrowness has been debated; two interpretations proposed so far have clearly different scenarios (e.g., Cassam-Chenaï et al. 2007). One considers the effect of a rapid decay of the amplified magnetic field downstream, so that bright narrow magnetic filaments are formed behind the shock (Pohl et al. 2005). The other assumes a relatively constant, strong magnetic field downstream of the shock. In this case, accelerated electrons quickly lose their energy through synchrotron radiation, resulting in narrow synchrotron X-ray filaments (e.g., Völk et al. 2005 and references therein). The nature of the magnetic-field amplification is not well understood at this time; the post-shock evolution of the field holds important clues to the process, so settling the question of the mechanism limiting filament widths has considerable significance.

Meanwhile, in RX J1713.7-3946 and Cas A SNRs, several synchrotron-dominated knotty features, whose size is about $10''$, were found to show year-scale time variations (e.g., Uchiyama et al. 2007; Patnaude & Fesen 2009). The rapid variations may reflect fast acceleration or cooling of accelerated electrons in strongly amplified magnetic fields up to the level

of mG. On the other hand, more diffuse regions in these SNRs do not show rapid variations, which leads the authors to consider that these regions have somewhat weaker magnetic fields. Thus, it is now possible to roughly estimate magnetic-field strengths, B , in SNRs, when time variations in synchrotron emission can be measured. Synchrotron X-ray flux variation can be produced stochastically, even in the absence of variations in the electron distribution, in the presence of a stochastic magnetic field (Bykov, Uvarov, & Ellison 2008). Somewhat smaller rms values of magnetic field are required, but substantial amplification is still necessary. (It should be noted that absence of variation does not demand low magnetic-field strengths; systematic, smooth steady-state magnetic-field amplification could produce steady emission varying only on overall SNR dynamical timescales, decades to centuries.)

In this paper, we investigate time variations of discrete features in the northeastern (NE) limb of SN 1006, using two *Chandra* observations taken in 2000 and 2008. We have recently measured proper motions of the shock fronts in the NE limb to be almost uniform at $0.''5 \text{ yr}^{-1}$ (Katsuda et al. 2009; hereafter Paper I). By correcting for the proper motion, we can track the same regions away from the shock front (or loosely, the same fluid elements) in two epochs. We also reveal detailed spatial structures of the synchrotron emission in the NE limb. Based on the results, we discuss why the synchrotron filaments are so narrow and the mechanism that limits the maximum energy of accelerated electrons.

2. Observations

We use two *Chandra* observations taken in 2000 (ObsID. 732) and 2008 (ObsID. 9107) that are the same data presented in our previous proper-motion measurements (Paper I). We use the reduced data products described in Paper I. We note that the second observation was specifically intended to allow a proper-motion measurement, and therefore the pointing direction, roll angle, and exposure time are the same as those in the first observation. This configuration was chosen to allow as precise a comparison in the two epochs as possible because the same physical regions are seen at almost the same detector position with the same effective area and spatial resolution.

3. Analysis and Results

Figure 1 (a) shows a three-color *Chandra* image of SN 1006, where red, green, and blue correspond to 0.5–0.8 keV (mostly, K-shell lines of O), 0.8–2.0 keV (mostly, Ne, Mg, and Si K lines), and 2.0–5.0 keV (mostly, synchrotron continuum) bands, respectively. Regions seen

in white are dominated by nonthermal synchrotron emission, while those in red or green are dominated by thermal emission. In this paper, we focus on the nonthermal emission, for which we will investigate time variations as well as detailed spatial structures.

As shown in Fig. 1 (b), we extract spectra from a number of small regions that are annular sectors covering the nonthermally-dominated area in the NE limb. We use the SNR center of $[(\text{ra}, \text{dec}) = (15^{\text{h}}02^{\text{m}}54^{\text{s}}.9, -41^{\circ}56'08''.9)$ (J2000)] determined from the *ROSAT* HRI image (Paper I). The sizes of the regions range from $10'' \times 30''$ to $15'' \times 115''$ to assure that each region contains about 3000 counts. There are 175 regions in all. For simplicity of our spectral analysis, we exclude boundary regions between the front- and back-illuminated chips (the boundaries are indicated as dashed lines in Fig. 1 (b)). Since we know that forward shocks in the NE limb are moving at $0''.5 \text{ yr}^{-1}$ (Paper I), we simply shift all the regions by $4''$ outward for the second observation. In this way, we extract two spectra (taken in 2000 and 2008) from each region. We subtract background emission from the source-free areas in the identical chip of the same observation. (The background never amounts to more than 15% of the total counts in a region, and is normally much less, so the use of χ^2 statistics is a reasonable approximation.) In addition to the X-ray data, we also use a VLA image at 1.37 GHz (Dyer et al. 2009) to constrain the normalization of nonthermal emission. We calculate radio fluxes from co-spatial regions, i.e., the small regions shifted by $2''$ outward compared with those for the first observations, since the radio image was taken in 2004. The radio resolution is $14'' \times 6''$ (long axis N-S), so the effect of this correction should be small.

Although most of the regions show featureless spectra, some regions exhibit K lines from metals such as O, Ne, Mg, or Si. We thus employ an absorbed nonthermal plus thermal components model, where we employ the **tbabs** model (Wilms et al. 2000) for absorption, the **srcut** model, which describes synchrotron emission from a power-law distribution of electrons with an exponential cut-off (Reynolds & Keohane 1999), with correction described in Reynolds 2008 for the nonthermal component, and the **vpshock** model, which describes thermal emission from a non-equilibrium ionization (NEI) plane-shock plasma, in conjunction with NEI version 2.0 (Borkowski et al. 2001) for the thermal component. In the fitting, photons in an energy range of 0.4–8.0 keV are used. We fix the intervening hydrogen column density, N_{H} , to be $6.8 \times 10^{20} \text{ cm}^{-2}$ (Dubner et al. 2002). In the **vpshock** component, we fix the abundances of O, Ne, Mg, and Si to be 4.4, 1.5, 15, and 50 times solar values (Anders & Grevesse 1989), respectively, following the most recent *XMM-Newton* results (Miceli et al. 2009). Other elemental abundances are fixed to solar values. The electron temperature, kT_e , and the ionization timescale, $n_e t$, are fixed to 0.5 keV and $1 \times 10^{10} \text{ cm}^{-3} \text{ sec}$, respectively (Miceli et al. 2009), where $n_e t$ is the electron density times the elapsed time after shock heating and the **vpshock** model assumes a range of $n_e t$ from zero up to $1 \times 10^{10} \text{ cm}^{-3} \text{ sec}$. Note that Miceli et al.’s results actually show that $kT_e \sim 0.4 \text{ keV}$ and $n_e t \sim 1.5 \times 10^{10} \text{ cm}^{-3} \text{ sec}$.

in the NE limb, but this parameter set does not affect our spectral-fit parameters presented below. The only free parameter we set in the **vpshock** model is the volume emission measure (VEM; $VEM = \int n_e n_H dV$, where n_H is the number density of protons, and V is the X-ray-emitting volume). For the **srcut** component, we let the cut-off frequency and the mean spectral index (the α parameter) inferred from the X-ray spectrum be free parameters, whereas the normalization (the flux at 1 GHz) is fixed to the value extrapolated from the radio flux at 1.37 GHz (Dyer et al. 2009) assuming a photon index of 0.55. In the initial fits, we allowed cut-off frequencies to vary freely in the two (2000 and 2008) data sets, but we found them to be consistent with each other. We thus simultaneously fit the 2000 and 2008 spectra, by linking all the spectral-fit parameters except for an additional parameter, the relative intensity of the **srcut** component between 2000 and 2008, which is allowed to vary freely so that we can measure time variations in its flux.

Figure 2 shows example spectra extracted from regions A (with no significant thermal emission) and B (with significant thermal emission) indicated in Fig. 1 (b). Black and red correspond to 2000 and 2008, respectively. The spectral difference between the two colors, which is clearly seen below 1 keV, shows the accumulation of molecular contaminants on the ACIS-S optical blocking filter. Also shown in the figure are the best-fit models and the residuals. Since the evolution of the contaminants is accounted for in the response files, the same model (with slightly adjusted intensity of the **srcut** component) fits both 2000 and 2008 data well. Spectral-fit parameters and fit statistics for the example spectra are summarized in Table 1. In this fitting procedure, a number of parameters for the thermal component are assumed and fixed. Although these values are plausible, it is worth checking the sensitivity of the fit results to varying these parameters. Before investigating, we first note that fit results for most of the regions are not sensitive to the treatments of thermal parameters since these regions are dominated by nonthermal emission like Region A (Fig. 2 left). On the other hand, the rest of the regions including Region B (Fig. 2 right), where contributions of the thermal emission are relatively large, could be affected by the assumptions in the fitting. We tried fitting the spectrum from Region B with $\pm 10\%$ different values for N_H , kT_e , and $n_e t$. We found that the fit results, i.e., the best-fit parameters in the **srcut** component, are not significantly changed from the original results listed in Table 1. Thus, variations of up to 10% in these parameters would not affect our results. We have also checked different sets of metal abundances. We examined three cases: (1) C=N=O=4.4, (2) Si=S=50, and (3) Fe=(Ni=)20 times the solar values, where the Fe abundance is based on the Fe-rich ejecta measured in the southeastern portion of SN 1006 with *Suzaku* (Yamaguchi et al. 2008). The first case yields a slightly better fit than the original fit, but the best-fit parameters are consistent with those in Table 1. The second case gave us almost the same results as those in Table 1, since S K lines are negligible for the assumed plasma conditions of (kT_e ,

$n_e t$) = (0.5 keV, $1 \times 10^{10} \text{ cm}^{-3} \text{ sec}$). In the third case, we find significantly different results: the photon index and the cut-off frequency are found to be 0.534 ± 0.007 and $2.3(\pm 0.2) \times 10^{16} \text{ Hz}$, respectively. However, the fit level ($\chi^2=158$) is not as good as that in Table 1. Therefore, we believe that the Fe abundance in the NE limb is more likely to be closer to the solar values rather than 20 times the solar values, and that our fitting procedure with the solar abundance for Fe is robust.

Maps of the the reduced χ^2 s, best-fit parameters (mean spectral index and cut-off frequencies), fluxes in the **srcut** component (2000 and 2008), and the flux ratios (2008/2000) are shown in Fig. 3 (a)–(f), where fluxes are calculated in the 0.4–8.0 keV band after correcting for interstellar absorption. Figure 3 (a) shows that the fits are fairly good for all the regions: the reduced χ^2 s are derived to be less than 1.5. We see relatively worse fits at the southern regions. This is because of the simplicity of the thermal model. Relatively large residuals are found around 0.7 keV energies where spectral modeling of the thermal emission is quite hard due to either missing K lines of O or inadequate atomic data for Fe L-shell lines (e.g., Yamaguchi et al. 2008). Also, such residuals are particularly evident in the southern regions where the contributions of thermal emission are relatively large compared with the rest of the regions. It is highly likely that this discrepancy does not affect the spectral-fit parameters in the nonthermal component. Therefore, we are confident of the best-fit parameters shown in Fig. 3.

As shown in Fig. 3 (b), mean spectral index are inferred to be around 0.5, which is consistent with the recent results from *Chandra* (Allen et al. 2008) and *XMM-Newton* (Miceli et al. 2009), but is slightly flatter than the radio value of 0.60 (0.51–0.68 for 90% C.L.) reported for the integrated spectrum (Allen et al. 2008). Our inferred mean spectral indices depend on flux ratios between radio and X-rays. Thus, systematic uncertainties of radio fluxes, which could originate from relatively worse spatial resolution of the radio image than that of the X-ray image, are subject to additional uncertainties of the mean spectral index. We check for the Region A spectrum that a 50% larger radio flux would yield a $\sim 5\%$ larger photon index. Therefore, together with the relatively large uncertainty ($\sim 15\%$) of the radio value from the integrated spectrum (Allen et al. 2008), we do not formally find significant inconsistency of the mean spectral index. Nonetheless, the best-estimated values show discrepancy, which would suggest a curved nonthermal spectrum expected in a nonlinear theory of diffusive shock acceleration (Reynolds & Ellison 1992), as previously noted by others (e.g., Allen et al. 2008). Cut-off frequencies in Fig. 3 (c) show strong variations in both radial and azimuthal direction. These spatial variations are also generally consistent with previous studies (Rothenflug et al. 2004; Allen et al. 2008; Miceli et al. 2009). We find a correlation between the cut-off frequency and the flux, for the first time. This will be briefly discussed in the next section. Detailed discussion about these spatial structures

will be published elsewhere.

We find flux maps of 2000 and 2008 to be quite similar to each other. This is confirmed by a flux ratio map in Fig. 3 (f), where most of the regions are in red (i.e., constant fluxes). In the figure, we see that a few northern regions show somewhat higher values (yellow color in Fig. 3 (f)) than the others. This is because of imperfect correction for the proper motions there; these regions have slightly larger proper motions than assumed here (see Paper I) and we checked that, if we choose spectral extraction regions more explicitly, we do not see flux variations. To study the flux variation more quantitatively, we plot the flux ratio (2008/2000) as a function of the flux in 2000 in Fig. 4 left. We can see that the data points are clustered tightly about a line representing no time variation. This means that the fluxes in 2000 and 2008 are quite similar with each other for most of the regions. On the other hand, it should be noted that there are a few data points showing relatively large variations of $\sim 20\%$. We can not rule out dramatic changes in those otherwise completely undistinguished regions, but we believe that the fluxes in these regions are not really changing. This is because some of them are expected to be due to imperfect corrections for the proper motions as mentioned above. And others are just statistical fluctuations, because (1) we have checked that these regions are randomly scattered (Fig. 3 (f)) and (2) the histogram of the flux ratio is well represented by a Gaussian function as shown in Fig. 4 right. In fact, if we apply a constant model to the flux ratios in Fig. 4 left, we obtain a fairly good fits of $\chi^2/\text{dof} = 157/174$ with a null hypothesis probability of 0.82. Thus, from a statistical point of view, we cannot reject the possibility that the fluxes are constant everywhere in the NE limb. Moreover, by looking at spectra from these regions, we see nothing special in their spectral features nor particular spectral parameters. In this context, we conclude that there are no peculiar regions showing strong time variations, and that all the regions show little or no time variations. We notice that the center of the histogram in Fig. 4 right is apparently shifted from unity: the Gaussian center is measured to be 0.977 ± 0.006 (90% C.L.).

The apparent decline in the global synchrotron flux is interesting, but falls within the calibration uncertainties for the effective area ($3\%^1$) determined by the CXC. Therefore, we have explored a variety of possibilities for improving the relative calibration of our measurement. There are relatively few point sources in the field, and these are not expected to be constant with time in any event. Indeed, the brightest source, QSO1 in Winkler et al. (2005) was brighter in 2008 by 50% than in 2000. A more promising alternative is to search for a change in the thermal emission and compare this to changes in the nonthermal emission.

Our strategy to estimate changes in nonthermal and thermal emission is as follows. We

¹http://web.mit.edu/iachec/IACHEC_2_talks/IACHEC.II_chandra_summary.pdf

first estimate nonthermal flux variations from the nonthermally-dominated regions (i.e., the outer regions elongated in the azimuthal direction in Fig. 1 (b)) as we have already analyzed. In this process, we assume no time variation for thermal emission to avoid possible degeneracy in separating thermal and nonthermal components; it is difficult to estimate the contribution of thermal emission correctly in these regions, and incorrect intensity ratios between the two epochs for thermal emission would affect those for nonthermal emission more or less. In any case, thermal emission makes only a small contribution in those regions. Next, we estimate thermal flux variations from thermally-dominated regions (i.e., interior regions elongated in the radial direction in Fig. 1 (b)). (Here, we assume the flux variation of nonthermal emission has the value measured above.) Spectra of these thermally-dominated regions are clearly distinct from those of the nonthermally-dominated regions (Fig. 2), resulting in different mean photon energies between them. To compare fluxes in these different kinds of spectra as accurately as possible, it may be important to consider the energy dependence of effective area and quantum efficiency. Therefore, we divide the spectra into three energy bands: 0.4–0.8 keV (K lines of O), 0.8–1.0 keV (K lines of Ne), and 1.0–8.0 keV. Finally, we compare flux variations between nonthermal and thermal emission in the three energy bands.

To measure flux variations in synchrotron emission of the three energy bands separately, we re-fit spectra from nonthermally-dominated regions. We employ the same model used above (i.e., `vps shock` plus `srcut`). We also treat the spectral-fit parameters in the same manner as above. The only exception is that the mean spectral indices are fixed to 0.5 which is typical in the NE limb (typical, if no spectral curvature is assumed) for relatively narrow energy bands of 0.4–0.8 keV and 0.8–1.0 keV where we cannot constrain both the photon index and the cut-off frequency (Note that, when fitting the 1.0–8.0 keV band, we allow the mean spectral indices to vary freely, since we can constrain them). As mentioned above, we assume no time variations for the thermal component. In this way, we fit all the spectra in the three energy bands, and derive statistically acceptable fits for them. Example spectra from region A indicated in Fig. 1 right are shown in Fig. 5 left. Then, fluxes of the nonthermal component are calculated from the best-fit models. Figure 6 (the first row) shows histograms of the flux ratios (2008/2000) for the three energy bands together with their best-fit Gaussian functions. The best-fit values of the Gaussian center are summarized in Table 2, from which we can see the energy dependence of the flux variations.

Next, we investigate flux variations in thermal emission. Since we were concerned that the thermally-dominated regions might not have the same proper motion as the synchrotron dominated regions, we examine four cases: 0'', 1'', 2'', and 3'' shifts in radial direction between the two epochs. It is also difficult to satisfactorily reproduce the thermal emission by plasma models (e.g., Yamaguchi et al. 2008). Therefore, we alternatively apply a phenomenological model consisting of several Gaussian components in addition to two bremsstrahlung com-

ponents plus an `srcut` component. The use of a phenomenological model is also justified by the fact that we are not trying to draw inferences from the model parameters but are just trying to get a good flux measurement. For the 0.4–0.8 keV band, we include five Gaussians at ~ 0.44 keV (N He α), ~ 0.5 keV (N Ly α), ~ 0.57 keV (O He α), ~ 0.66 keV (O Ly α and O He β), and ~ 0.7 keV (O He γ and/or Fe L). For the 0.8–1.0 keV band, we include two Gaussians at ~ 0.71 keV (O He δ) and ~ 0.91 keV (Ne He α). For the 1.0–8.0 keV band, we include three Gaussians at ~ 1.35 keV (Mg He α), ~ 1.8 keV (Si He α), and ~ 2.4 keV (S He α). Center energies, widths, and normalizations in the Gaussian components are treated as free parameters, but for those at 0.7 keV and 0.71 keV, only normalizations are allowed to vary freely with fixed center energies and fixed widths at zero. We fix kT_{e} s in the two bremsstrahlung components to 0.5 keV and 2.0 keV, based on recent X-ray analyses from *Suzaku* (Yamaguchi et al. 2008) and *XMM-Newton* (Miceli et al. 2009). In the `srcut` model, the mean spectral index is fixed to 0.5. The normalization is also fixed to the value estimated from the 1.37 GHz image. The cut-off frequency is left as a free parameter. The relative intensity of the `srcut` model between the two epochs is fixed to those derived in the previous paragraph (see, Table 2), whereas that of the thermal component (i.e., the sum of all the components excluding the `srcut` component) is allowed to vary freely so that we can obtain its flux variation. This model yields statistically acceptable fits for all the spectra in the three energy bands. Example spectra from region C indicated in Fig 1 right are shown in Fig. 5 right. Similarly to the nonthermally-dominated regions, we generate flux-ratio histograms of the thermal component as shown in Fig. 6, where the second, third, fourth, and fifth rows are responsible for 0'', 1'', 2'', and 3'' shifted cases, respectively. The values of the best-fit Gaussian centers are summarized in Table 2.

Looking at Table 2, we see that there are flux changes in both the thermal and non-thermal emission and that the changes in the two components. In fact, ratios of the flux variations between nonthermal and thermal emission are calculated to be about unity at all the three energy bands as also shown in Table 2. This is strong evidence that the changes in flux are due to calibration effects.

Can the flux changes in both the thermal and nonthermal emission be understood? The fluxes increase by $\sim 3\%$ at low energies whereas they decrease by $\sim 4\%$ at high energies. Also notable in the table is energy dependence of flux variations: the fluxes increase by $\sim 3\%$ at low energies, whereas they decrease by $\sim 4\%$ at high energies. Since the contaminants on the optical blocking filter could influence spectra below 1 keV, the increasing flux at low energies could be due to this effect. On the other hand, it cannot fully explain the decreasing flux at high energies.

There are two possibilities for the variations at high energies. One is that some calibra-

tion effects cause the apparent changes for both thermal and nonthermal emission, i.e., the fluxes are actually almost constant with time. In this case, the time variation of nonthermal emission would be less than 1% over 8 yrs, based on the time-variation ratio between nonthermal and thermal measured in 1–8 keV (see, Table 2). This interpretation is supported by the fact that flux variations of thermal emission are in good agreement with those of nonthermal emission; it is likely that the agreements are not just coincidence but that they have the same underlying origin. As an additional check of calibration effects, we compared two observations of clusters of galaxies, since they are not expected to change over the time period of interest (i.e., ~ 10 yrs). We chose the Fornax cluster and HCG62, since they were observed twice over this time period with the same chip (i.e., chip7) on the ACIS-S array. We found that both of them are apparently declining: $\sim 7\%$ between 2000 and 2009 for the Fornax cluster and $\sim 3\%$ between 2000 and 2008 for HCG62. This result implies the presence of calibration effects. Given that we measure relative fluxes between 2000 and 2008, we need time-dependent calibration effects to explain the flux variations seen. These effects includes the buildup of the ACIS contaminant, the increase in charge transfer inefficiency which could result in $\lesssim 1\%$ uncertainty in flux measurements, and the variable particle background which could result in $\sim 1\%$ uncertainty in flux measurements (a private communication with Paul Plucinsky). To estimate the flux uncertainty from contaminants, we use the `acisabs` model in XSPEC with response files without corrections for the effects of contaminants. This model allows us to examine various amounts of contaminants by specifying various time since the launch of *Chandra* in its parameter. We find that a 10% variation of the quantum efficiency at 0.67 keV would result in a 1% variation of the flux in 1–8 keV for a nonthermally-dominated spectrum. Therefore, calibration uncertainties in relative fluxes could be as large as $\sim 3\%$, consistent with our measurements. We conclude that the time variation in the flux from synchrotron emission is most likely constant to 1%, and certainly less than 1%.

However, we cannot fully rule out the other possibility that both thermal and nonthermal emission are declining at similar rates by chance. Therefore, it is interesting to investigate the time variation from a theoretical point of view. Simple models for the evolution of synchrotron brightness of SNRs (e.g., Reynolds & Chevalier 1981) predict the rate at which synchrotron flux should be dropping. As shown in the Appendix A, assuming as in that paper that both magnetic-field energy density and relativistic-electron energy density scale with postshock pressure $P \propto \rho u_s^2$, but generalizing from the assumption of Sedov evolution made there to the observed expansion rate $R \propto t^m$ with $m = 0.54$ (Paper I), we predict that above the cut-off frequency ν_{cutoff} the synchrotron intensity should drop off at $(0.2 - 0.25)\% \text{ yr}^{-1}$ ($1.6\% - 2.0\%$ between 2000 and 2008), of the same order as the small variation we find. The thermal emission should change, too. However, as it depends on NEI effects, etc., modeling its time variation is much harder and is beyond the scope of this paper. Without

estimates of the time variation for thermal emission, we leave it open whether the rate of the time variation over 8 yrs is at $\sim 4\%$ or less than 1%, or whether the entire effect is due to calibration uncertainties.

4. Discussion

We have investigated time variations of discrete regions in the NE limb of SN 1006, using two *Chandra* observations taken in 2000 and 2008. We found that there are no particular features showing strong time variations, and that the synchrotron emission stays at constant within 4% and probably with 1% over the time span. This result distinguishes SN 1006 from core-collapse SNRs such as RX J1713.7-3946 and Cas A in which several hot spots show year-scale time variations of a factor ~ 2 or more (e.g., Uchiyama et al. 2007). To understand the cause of the difference between SN 1006 and others, it should be noted that there are no knotty features in the SN 1006 NE limb. In fact, diffuse regions in RX J1713.7-3946 and Cas A do not show fast time variations, either. This suggests that rapid time variations are only observed in bright knotty features. Such a situation is indeed predicted by a recently proposed theory that interactions between SNR shocks and ambient small-scale cloudlets amplify magnetic fields through plasma instabilities, and resultant strongly magnetized features (which appears as knots or filaments) show rapid brightness changes (Giaccalone & Jokipii 2007; Inoue et al. 2009). In this view, the fact that we do not find knotty features which could show rapid time variations in SN 1006 is reasonably interpreted as it is located at high Galactic latitude where small-scale cloudlets are not present. Additionally, SN 1006 as a Type Ia remnant is interacting with undisturbed ISM instead of the stellar wind of the progenitor as is likely for the other two objects, and massive-star winds may be quite clumpy. Further investigations for the rest of the limb of SN 1006 and other SNRs will be good opportunities to test the scenario for the origin of rapid time variations in terms of amplification of magnetic fields.

Our failure to find strong time variability in the synchrotron emission from SN 1006 is consistent with the absence of small structures in its morphology. While significant brightness changes on a timescale of a few years may be explained as electron acceleration or synchrotron-loss timescales, requiring magnetic field strengths of $0.1 - 1$ mG (e.g., Uchiyama et al. 2007), the absence of such changes does not require that the magnetic fields be weak. Steady-state particle acceleration at the shock, followed by downstream convection in the presence of energy losses, would result in synchrotron flux varying only on the timescales estimated in the Appendix A, which are independent of B and depend only on the shock deceleration rate. The absence of strong variability in SN 1006 may then be explained by its

being a remnant of a Type Ia supernova, expanding into relatively uniform material. The high magnetic fields estimated assuming filament thicknesses are set by synchrotron losses ($B \sim 100 \mu\text{G}$, e.g., Vink & Laming 2003; Morlino et al. 2010; Ksenofontov et al. 2005) are not in contradiction with our result of little flux variability.

We also revealed spatial structures of the synchrotron emission in unprecedented detail, and found a correlation between the flux and the cut-off frequency. Given that the flux likely depends on the magnetic field, the simplest explanation is that the cut-off frequency depends on the magnetic field as well, so that the magnetic field controls spatial structures of both the flux and the cut-off frequency. This is important in understanding the mechanism limiting the maximum energy, E_{max} , of accelerated particles in SN 1006. If the SNR age and/or escape of particles limit E_{max} , then $E_{\text{max}} \propto B$ (Reynolds 2008). In this case, the cut-off frequency, which is proportional to $E_{\text{max}}^2 B$, goes as B^3 . On the other hand, if radiative losses limit E_{max} , then $E_{\text{max}} \propto B^{-0.5}$, canceling the B -dependence of the cut-off frequency. Therefore, the possible B -dependence of the cut-off frequency we found suggests that synchrotron radiative losses do not limit E_{max} in the SN 1006 NE limb. This would mean that the observed E_{max} of electrons would apply to ions as well. Using the highest cut-off frequency of $\sim 2 \times 10^{17} \text{Hz}$ at the outermost regions and a magnetic field just behind the shock of $90 \mu\text{G}$ (Morlino et al. 2010), we estimate E_{max} to be $\sim 12(\nu_{\text{cutoff}}/2 \times 10^{17} \text{Hz})^{0.5} (B/90 \mu\text{G})^{-0.5} \text{TeV}$. We note that it is also possible that some additional physical effect, for instance a dependence on the obliquity angle between the shock velocity and upstream magnetic field, affects both electron injection and acceleration rate. In the presence of such an effect, radiative losses might still be the operative limitation on the electron spectrum. Another interpretation for the correlation between the flux and the cut-off frequency is discussed in the Appendix B.

5. Conclusion

We tracked time variations in synchrotron flux of discrete regions in the SN 1006 NE limb from two *Chandra* observations in 2000 and 2008. Unlike core-collapse SNRs RX J1713.7-3946 and Cas A where year-scale variations were found in small-scale knotty structures (e.g., Uchiyama et al. 2007; Patnaude & Fesen 2009), we found that the X-ray emission from the SN 1006 NE limb is quite steady. We set the upper limit of global time variations in the NE limb to be 4% and most likely 1% over 8 yrs. While simple considerations lead to a prediction of a decline of 1 – 2% over this period, calibration uncertainties are also of comparable size. We also revealed detailed spatial structures of the synchrotron emission. We found a correlation between the flux and the cut-off frequency, which suggests that the maximum energy of accelerated electrons is not limited by synchrotron losses. If this is the

case, the maximum energy for electrons, which we calculate to be ~ 12 TeV, would be the same as that for ions. The correlation might also point to new physical effects on electron injection or acceleration. In conclusion, we found no indications of particle acceleration or synchrotron losses in discrete features in the SN 1006 NE limb.

We acknowledge helpful scientific discussions with Una Hwang. We are grateful to Paul Plucinsky and Alexey Vikhlinin for discussion of the *Chandra* ACIS calibration. S.K. is supported by a JSPS Research Fellowship for Research Abroad, and in part by the NASA grant under the contract NNG06EO90A. P.F.W. acknowledges the support of the NSF through grant AST 0908566.

6. Appendix A

We can estimate the expected rate of change of X-ray synchrotron flux from SN 1006 with a very simple model, emission from a homogeneous region just behind the shock whose synchrotron radiation is produced by a power-law distribution of electrons with an exponential cutoff at an energy E_{\max} . We shall assume that the shock puts a constant fraction of post-shock energy density into relativistic electrons and another constant fraction into magnetic-field energy. As the shock decelerates, these energies decrease, resulting in a decrease in the synchrotron emissivity at low energies but also a drop in E_{\max} , giving a faster rate of decrease at photon energies produced by electrons with $E > E_{\max}$. As the remnant radius R increases, however, the intensity along a line of sight I_ν grows as R . Of course the true situation is much more complex, but these simple considerations allow for an estimate.

The synchrotron emissivity from an exponentially truncated power-law distribution of electrons $N(E) = KE^{-s}e^{-E/E_{\max}}$ between E_l and $E_h > E_{\max}$ is given approximately by

$$j_\nu = c_j(\alpha)KB^{1+\alpha}\nu^{-\alpha}\exp(-\sqrt{\nu/\nu_c}) \quad (1)$$

where $\alpha = (s - 1)/2$ and $\nu_c \equiv c_1 E_{\max}^2 B$ ($c_1 \equiv 1.82 \times 10^{18}$ cgs; $c_j(0.6) = 3.48 \times 10^{-12}$). In general, $c_j \equiv c_5(\alpha)(2c_1)^\alpha$ in the notation of Pacholczyk (1970), with $c_5(0.6) = 1.17 \times 10^{-23}$. The intensity along a line of sight is $I_\nu = \int j_\nu dl \cong j_\nu L \propto j_\nu R$. We take $\alpha = 0.6$, roughly the radio value, although the results are not highly sensitive to α .

We consider a spherical evolving supernova remnant of radius $R \propto t^m$ and shock speed $u_s \equiv dR/dt = mR/t \propto t^{m-1}$, expanding into a uniform medium of density ρ . We assume that the shock puts a constant fraction of post-shock thermal energy ($\propto \rho u_s^2$) into relativistic electrons:

$$u_e \equiv \int_{E_l}^{E_h} N(E) dE \cong \frac{K}{s-1} (E_l^{1-s} - E_{\max}^{1-s}) \cong \frac{K}{s-1} E_l^{1-s} \quad (2)$$

where we have assumed $E_l \ll E_{\max}$. Then if $E_l = \text{const.}$, $K \propto u_e \propto u_s^2 \propto t^{2m-2}$. Next we assume that the magnetic energy density $B^2/8\pi$ is amplified to a (probably different) constant fraction of ρu_s^2 : $B^2 \propto u_s^2 \Rightarrow B \propto u_s \propto t^{m-1}$.

For energies far below the cutoff energy E_{\max} (i.e., at observing frequencies $\nu \ll \nu_c$), we can find the time-dependence of the intensity I_ν along any given line of sight:

$$I_\nu \propto j_\nu R \propto t^{2m-2} t^{(m-1)(1+\alpha)} t^m = t^{(m-1)(3+\alpha)+m}. \quad (3)$$

For SN 1006, in the NE, $m = 0.54$ (Paper I). Then for $\alpha = 0.6$,

$$I_\nu(\nu \ll \nu_c) \propto t^{(-0.46)(3.6)+m} = t^{-1.12} \equiv t^p. \quad (4)$$

Then the prediction for the decay of synchrotron emission below ν_c , for instance in the radio, is

$$\frac{1}{I_\nu} \frac{dI_\nu}{dt} = \frac{p}{t} = -0.11\% \text{ yr}^{-1}, \quad (5)$$

or a total drop of 0.89% in 8 years.

However, as we are considering the 1–8 keV continuum, and our fitted values for $h\nu_c$ are typically below 1 keV ($\nu_c < 2.4 \times 10^{17}$ Hz), we need to consider the time-dependence of ν_c , i.e., of E_{\max} . If acceleration is limited by synchrotron losses, $E_{\max} \propto B^{-1/2} u_s$, and $\nu_c \propto E_{\max}^2 B \propto u_s^2 \propto t^{2m-2}$. In any case, let $\nu_c = \nu_0(t/t_0)^n$.

Then, writing $I_\nu = I_0(t/t_0)^p e^{-\sqrt{\nu/\nu_c(t)}}$,

$$\frac{dI_\nu}{dt} = I_\nu \left(\frac{p}{t} + \frac{n}{2t} \sqrt{\frac{\nu}{\nu_c}} \right). \quad (6)$$

For SN 1006, $\nu_c \sim 2 \times 10^{17}$ Hz in the synchrotron-bright NE, so taking a mean photon energy of about 4 times that (3.3 keV), and using $n = 2m - 2 = -0.92$ and $p = -1.12$ as above,

$$\frac{1}{I_\nu} \frac{dI_\nu}{dt} = \frac{1}{t} (p + n) = \frac{-2.04}{1000} \Rightarrow -0.20\% \text{ yr}^{-1} \quad (7)$$

or about –1.6% over 8 years. A more careful integration over the curved spectrum between 1 and 8 keV shouldn't change this estimate by much.

If, alternatively, the acceleration is limited by the finite age of SN 1006, we have $E_{\max} \propto B u_s 2t \Rightarrow \nu_c \propto B^3 u_s^4 t^2 \propto t^{7(m-1)+2} = t^{-1.22}$ and

$$\frac{1}{I_\nu} \frac{dI_\nu}{dt} = \frac{-2.34}{1000} \Rightarrow -0.23\% \text{ yr}^{-1} \quad (8)$$

or about -1.9% over 8 years.

For completeness, a third alternative is the escape of particles above some energy, perhaps due to absence of MHD waves to scatter them. Then, if waves disappear above some wavelength λ_m , $E_{\max} \propto \lambda_m B \Rightarrow \nu_c \propto \lambda_m^2 B^3 \Rightarrow n = 3(m - 1)$ (ignoring possible evolutionary changes to λ_m). This gives $n = -1.38$ and

$$\frac{1}{I_\nu} \frac{dI_\nu}{dt} = \frac{-2.5}{1000} \Rightarrow 0.25\% \text{ yr}^{-1} \quad (9)$$

or about -2.0% over 8 years.

7. Appendix B

Now the acceleration rate is proportional to the diffusion coefficient $\kappa = \lambda_{\text{mfp}} c/3$, where the mean free path λ_{mfp} is normally taken to be proportional to the gyroradius, $\lambda_{\text{mfp}} = \eta r_g = \eta E/eB$ (the last equality applying in the extreme-relativistic limit). In the “quasi-linear” approximation, $\eta = (\delta B/B)^{-2}$, where δB is the magnitude of resonant MHD fluctuations. (The “Bohm limit” is $\eta = 1$ or $\lambda_{\text{mfp}} = r_g$; constant η at some other value > 1 is termed “Bohm-like.” Constant η corresponds to a “white noise” spectrum of MHD waves, equal energy in all decades of wavenumber: if $I(k)dk$ is the energy in waves with wavenumbers in dk , $I \propto k^{-1}$.) While most workers assume Bohm-like or Bohm-limit diffusion (e.g., Berezhko, Ksenofontov, & Völk 2009), one could imagine a departure from this assumption; to produce the correlation we observe, it would be necessary to have η decrease with B (i.e., one needs more rapid acceleration where the field is stronger). To our knowledge, there is at present no theoretical prediction of such an effect, but it might exist. However, it can be shown (Reynolds 2004) that the most straightforward generalization, in which η depends on E because the turbulent spectrum of MHD waves has a different slope, $I(k) \propto k^{-n}$ with $n \neq 1$, produces the wrong correlation. In this case, the acceleration time to energy E , $\tau(E)$, obeys $\tau(E) \propto E^\beta/B$ where $\beta = 2 - n$. Then $\beta = 1$ is the Bohm limit. The value of β depends on the nature of the scattering medium; for scattering by MHD waves with a Kolmogorov spectrum, $n = 5/3$ so $\beta = 1/3$, and normal turbulent spectra are expected to be steep, $n > 1 \Rightarrow \beta < 1$. Equating $\tau(E)$ to the synchrotron loss time gives the maximum energy of loss-limited acceleration $E_{\max}(\text{loss}) \propto B^{-[1/(1+\beta)]}$, and corresponding cut-off frequency $\nu_c \propto B^{(\beta-1)/(\beta+1)}$. (So for Bohm-like diffusion, $\eta = \text{constant}$ or $\beta = 1$, there is no B -dependence. Models in which turbulence is generated by the cosmic rays themselves typically produce Bohm-like diffusion.) If $\beta < 1$, higher B lowers the cut-off frequency, producing the opposite correlation to the one we observe. However, it is still possible that some as yet unknown effect produces turbulence with highest power at short wavelengths,

$n < 1 \Rightarrow \beta > 1$. In this unlikely case, brighter regions would be expected to have higher cut-off frequencies as observed, due to variations in B . That, or some other alteration to the standard diffusion picture, could allow acceleration to be loss-limited. It must be noted, however, that increasing η above 1 in some parts of the shock lowers the maximum energy to which particles of any species can be accelerated there, and may impact the ability of shocks to produce the highest-energy Galactic cosmic ray ions.

Table 1. Spectral-fit parameters for example spectra in regions A and B

Parameters	Region A	Region B
N_H (10^{20} cm $^{-2}$)	6.8 (fixed)	6.8 (fixed)
srcut component		
Constant factor (2008/2000)	1.00 ± 0.05	0.91 ± 0.08
Mean spectral index	$0.502^{+0.004}_{-0.005}$	$0.503^{+0.007}_{-0.006}$
Cut-off frequency (10^{16} Hz)	19^{+2}_{-4}	1.6 ± 0.1
Flux at 1 GHz (Jy arcmin $^{-2}$)	0.236 (fixed)	0.052 (fixed)
vpshock component		
kT_e (keV)	0.5 (fixed)	0.5 (fixed)
$\log(n_e t/\text{cm}^{-3} \text{ sec})$	10 (fixed)	10 (fixed)
O	4.4 (fixed)	4.4 (fixed)
Ne	1.5 (fixed)	1.5 (fixed)
Mg	15 (fixed)	15 (fixed)
Si	50 (fixed)	50 (fixed)
$\int n_e n_H dl^a$ (10^{16} cm $^{-5}$)	0.5 ± 0.3	12 ± 1
$\chi^2/\text{d.o.f.}$	132/169	141/104

Note. — Errors indicate the 90% confidence ranges. Abundances not listed are fixed to the solar values. ^aVEM normalized by the region area; dl is the plasma depth.

Table 2. Flux ratios (2008/2000)

	0.4–0.8 keV	0.8–1.0 keV	1.0–8.0 keV
Nonthermal	1.028 ± 0.012	0.962 ± 0.011	0.964 ± 0.006
Thermal (no shift)	1.021 ± 0.010	0.968 ± 0.022	0.947 ± 0.016
Thermal (1'' shift)	1.026 ± 0.010	0.975 ± 0.021	0.956 ± 0.014
Thermal (2'' shift)	1.031 ± 0.010	0.991 ± 0.016	0.966 ± 0.013
Thermal (3'' shift)	1.035 ± 0.011	0.988 ± 0.022	0.972 ± 0.012
Thermal (mean)	1.028 ± 0.010	0.982 ± 0.020	0.961 ± 0.016
Nonthermal / Thermal	0.997 ± 0.015	0.980 ± 0.023	1.003 ± 0.018

Note. — Errors indicate the 90% confidence ranges.

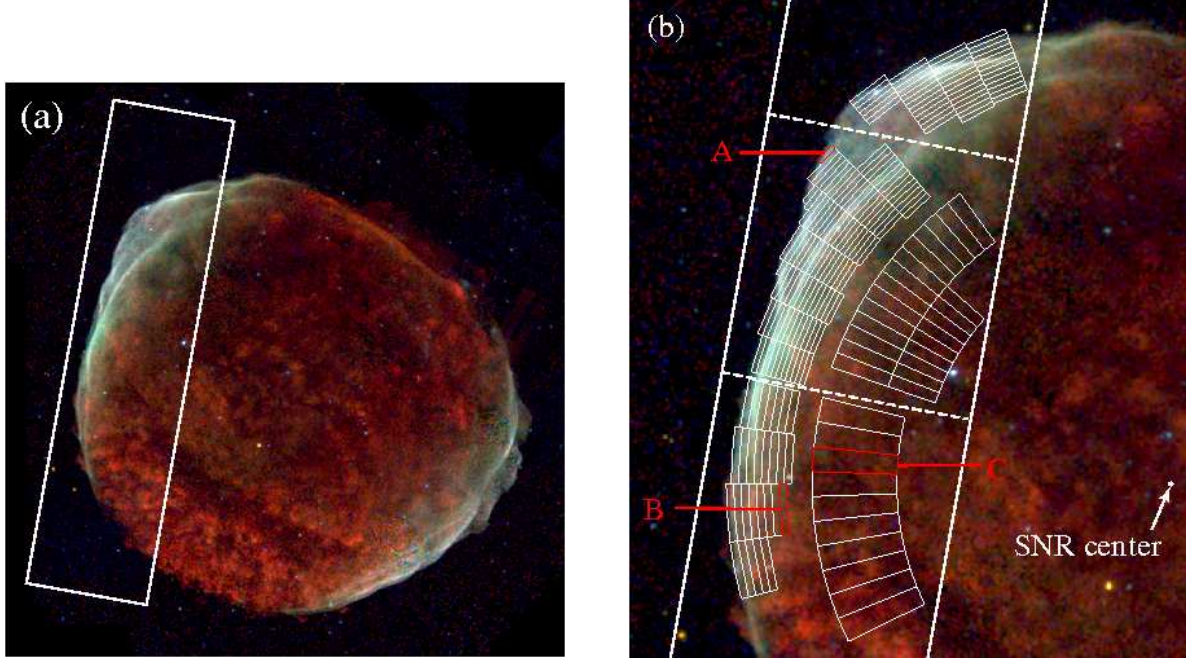


Fig. 1.— (a) *Chandra* three-color image after vignetting effects are corrected. Red, green, and blue correspond to 0.5–0.8 keV (mostly, K lines of O), 0.8–2.0 keV (mostly, K lines of Ne, Mg, and Si), and 2.0–5.0 keV (mostly, synchrotron emission) bands, respectively. The image is binned by $1''.97$ and has been smoothed by a Gaussian kernel of $\sigma = 5''.90$. The intensity scale is square root. The field of view of the *Chandra* observations of the NE limb (ObsIDs 732 and 9107) are shown as a white box. (b) Same as Fig. 1 (a), but focused on the NE limb. The field of view the *Chandra* observations are within two white lines. We extract spectra from white (and red) pie-shaped regions. Example spectra for red regions indicated as letters A–C are shown in Figs. 2 and 5. The SNR center of $[(\text{ra}, \text{dec}) = 15^{\text{h}}02^{\text{m}}54^{\text{s}}.9, -41^{\circ}56'08''.9 \text{ (J2000)}]$ is taken from Paper I.

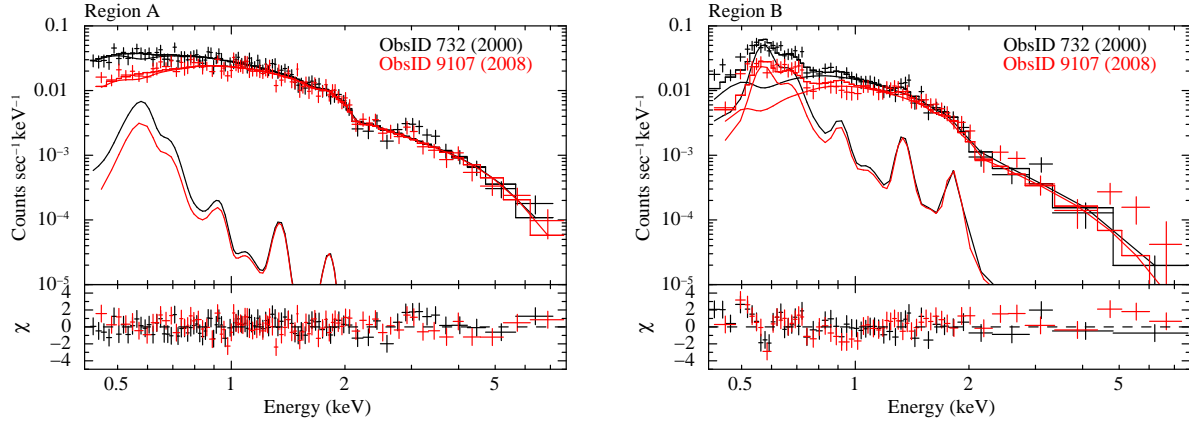


Fig. 2.— Left: Example spectra extracted from region A indicated in Fig. 1 along with the best-fit models and the residuals. Black and red correspond to the 2000 and 2008 data, respectively. Components of nonthermal and thermal emission are separately illustrated. Right: Same as left but for region B indicated in Fig. 1.

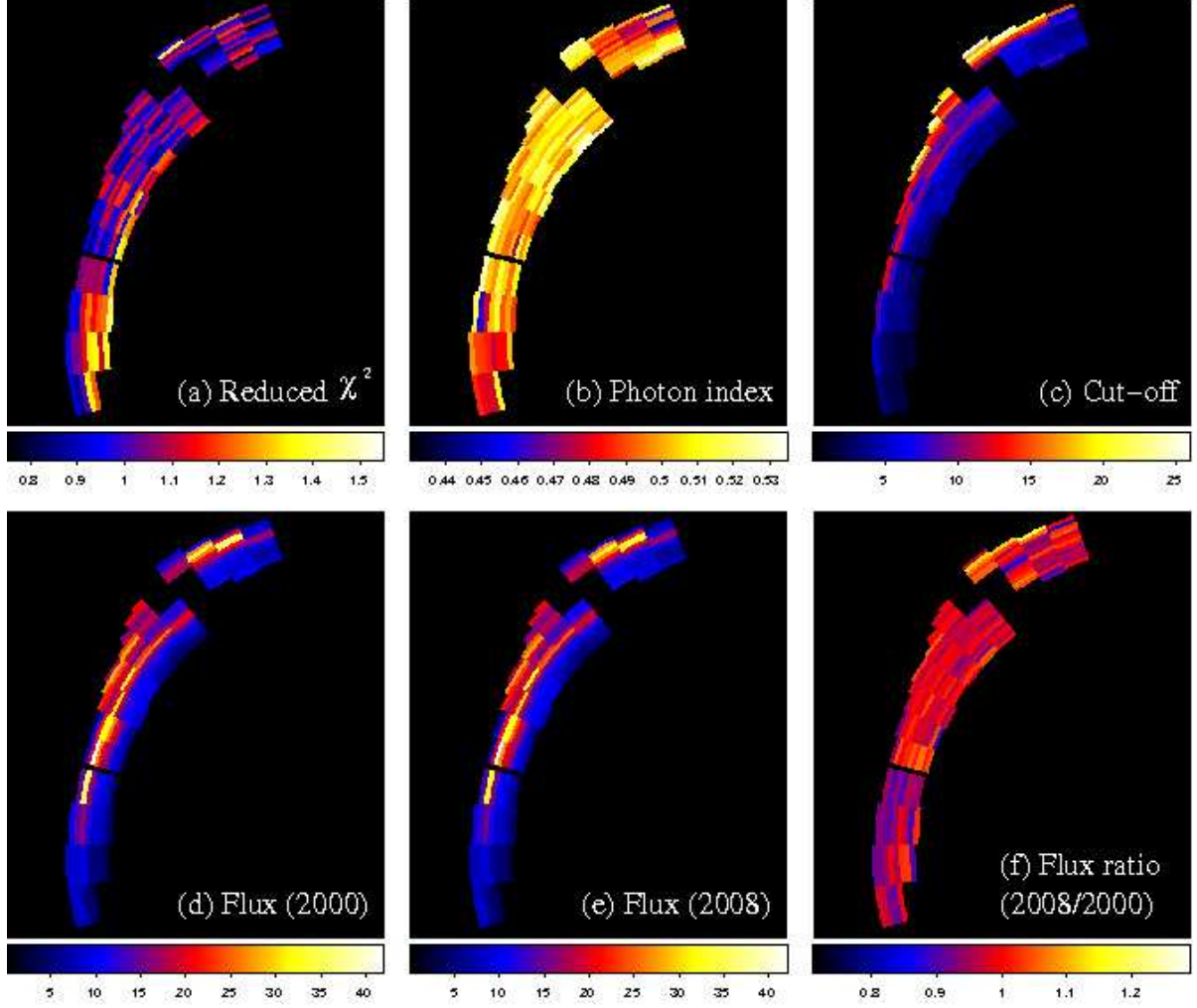


Fig. 3.— Results from the spatially-resolved spectral analysis for the nonthermally-dominated regions. Panels (a)–(f) show distributions of reduced χ^2 s, mean spectral indices inferred from the X-ray spectra, cut-off frequencies, fluxes corrected for the interstellar absorption in 0.4–8.0 keV for 2000 and 2008, and the flux ratios, respectively. Values of the cut-off frequencies and fluxes are in units of 1×10^{16} Hz and 1×10^{-13} ergs cm $^{-2}$ sec $^{-1}$ arcmin $^{-2}$, respectively.

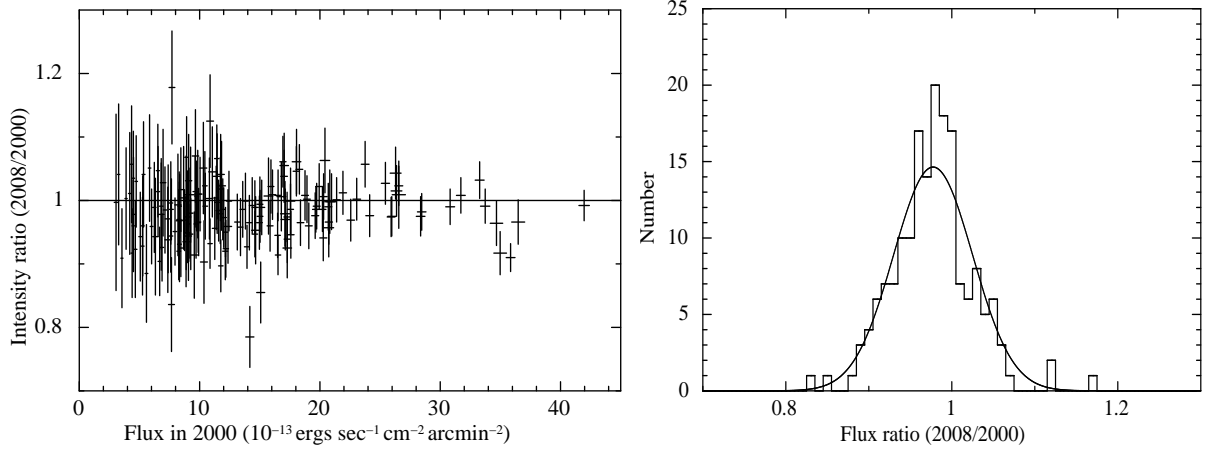


Fig. 4.— Left: Flux ratio in the `srcut` component as a function of the flux in 2000. Errors of the vertical axis are 90% confidence ranges of the constant parameters for the `srcut` component, while those of the horizontal axis are square root of photon numbers in the `srcut` component. A horizontal solid line drawn in the figure represent a constant flux line. Right: Histogram of flux ratios (2008/2000). The best-fit Gaussian function is shown together.

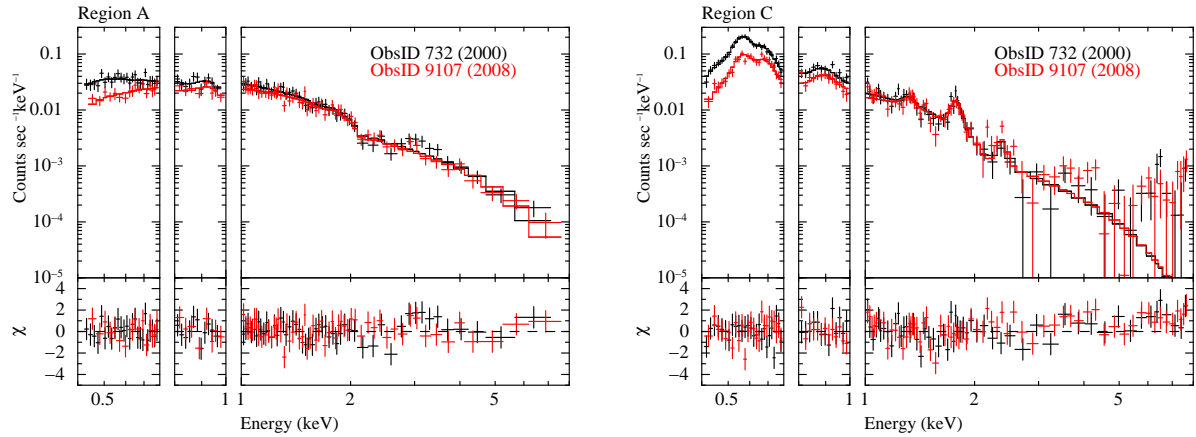


Fig. 5.— Left: Same as Fig. 2 left, but the spectra are fitted separately in energy bands of 0.4–0.8 keV, 0.8–1.0 keV, and 1.0–8.0 keV. Right: Same as left but for a thermally-dominated region, region C indicated in Fig. 1.

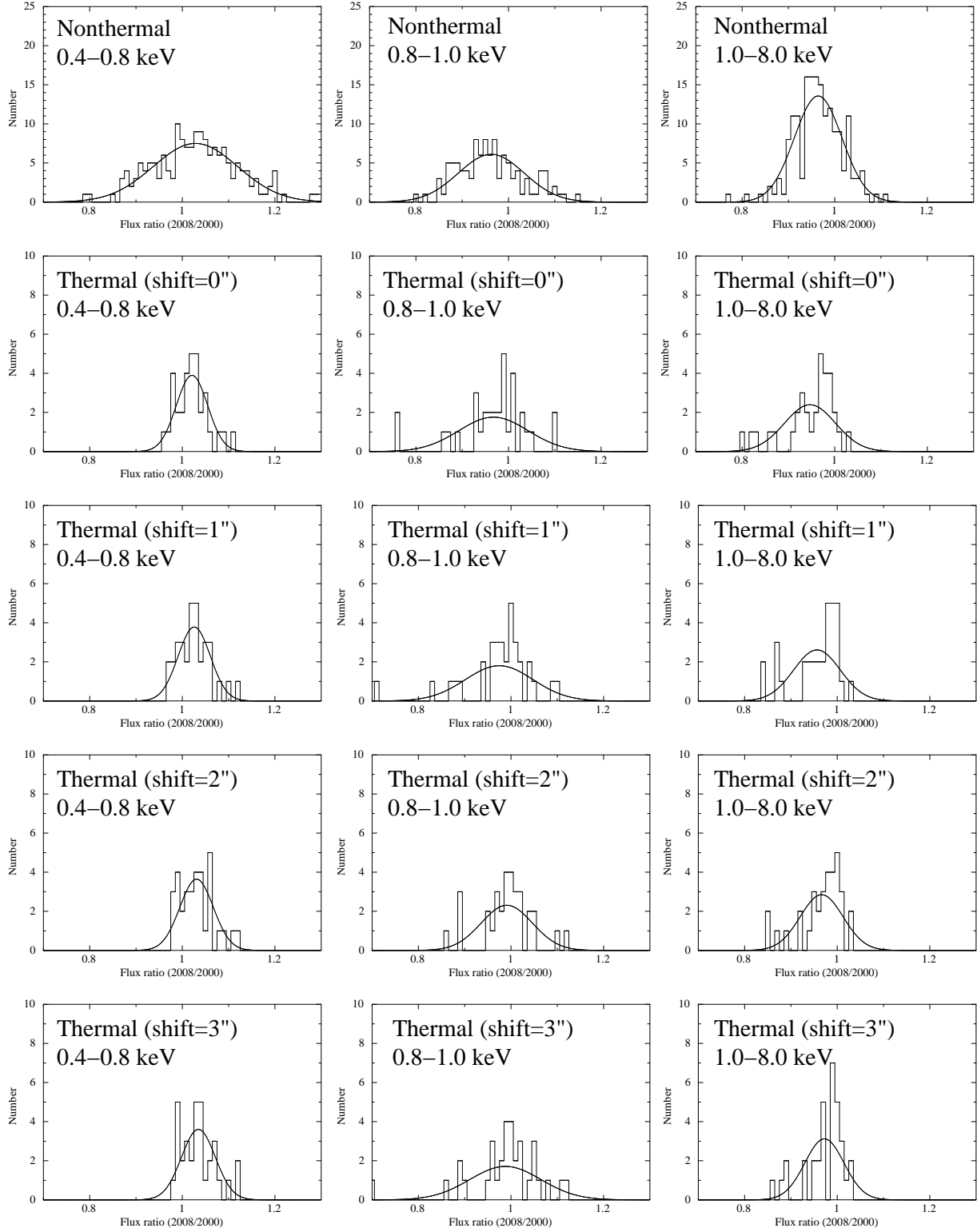


Fig. 6.— Histograms of flux ratios (2008/2000) for energy bands of 0.4–0.8 keV (left column), 0.8–1.0 keV (middle column), and 1.0–8.0 keV (right column). The first row is responsible for nonthermally-dominated regions, while others are responsible for thermally-dominated regions.

REFERENCES

- Acero, F., et al. 2010, *A&A*, 516, 62
- Allen, G. E., Houck, J. C., Sturmer, S. J. 2008, *ApJ*, 683, 773
- Anders, E., & Grevesse, N. 1989, *Geochim. Cosmochim. Acta*, 53, 197
- Bamba, A., Yamazaki, R., Ueno, M., & Koyama, K. 2003, *ApJ*, 589, 827
- Bamba, A., Yamazaki, R., Yoshida, T. Terasawa, T., & Koyama, K. 2005, *ApJ*, 621, 793
- Berezhko, E. G., Ksenofontov, L. T., & Völk, H. J. 2009, *A&A*, 505, 169
- Borkowski, K. J., Lyerly, W. J., & Reynolds, S. P. 2001, *ApJ*, 548, 820
- Bykov, A. M., Uvarov, Y. A., Ellison, D. C. *ApJ*, 689, L133
- Cassam-Chenaï, G., Hughes, J. P., Ballet, J., and Decourchelle, A. 2007, *ApJ*, 665, 315
- Dubner, G. M., Giacani, E. B., Goss, W. M., Green, A. J., Nyman, L-A. 2002, *A&A*, 387, 1047
- Dyer, K. K., Cornwell, T. J., Maddalena, R. J. 2009, *AJ*, 137, 2956
- Giacalone, J., & Jokipii, J. R. 2007, *ApJ*, 663, L41
- Inoue, T., Yamazaki, R., Inutsuka, S. 2009, *ApJ*, 393, 1377
- Katsuda, S., Petre, R., Long, K. S., Reynolds, S. P., Winkler, P. F., Mori, K., & Tsunemi, H. 2009, *ApJ*, 692, L105 (Paper I)
- Koyama, K., Petre, R., Gotthelf, E. V., Hwang, U., Matsuura, M., Ozaki, M., Holt, S. S. 1995, *Nature*, 378, 255
- Ksenofontov, L. T., Berezhko, E. G., & Völk, H. J. 2005, *A&A*, 443, 973
- Long, K. S., Reynolds, S. P., Raymond, J. C., Winkler, P. F., Dyer, K. K., Petre, R. 2003, *ApJ*, 586, 1162
- Miceli, M., Bocchino, F., Iakubovskiy, D., Orlando, S., Telezhinsky, I., Kirsch, M. G. F., Petruk, O., Dubner, G., & Castelletti, G. 2009, *A&A*, 501, 239
- Morlino, G., Amato, E., Blasi, P., & Caprioli, D. 2010, *MNRAS*, 405, L21
- Pacholczyk, A. G. 1970, *Radio Astrophysics* (San Francisco: Freeman)

- Patnaude, D. J., & Fesen, R. A. 2009, *ApJ*, 697, 535
- Pohl, M., Yan, H., & Lazarian, A. 2005, *ApJ*, 626, L101
- Reynolds, S. P., & Chevalier, R. A. 1981, *ApJ*, 245, 912
- Reynolds, S. P., & Ellison, D. C. 1992, *ApJ*, 399, L75
- Reynolds, S. P., 1998, *ApJ*, 493, 375
- Reynolds, S. P., 2004, *Adv. Space Res.*, 33, 461
- Reynolds, S. P., 2008, *ARA&A*, 46, 89
- Rothenflug, R., Ballet, J., Dubner, G., Giacani, E., Decourchelle, A., & Ferrando, P. 2004, *A&A*, 425, 121
- Uchiyama, Y., Aharonian, F. A., Tanaka, T., Takahashi, T., & Maeda, Y. 2007, *Nature*, 449, 576
- Uchiyama, Y., Aharonian, F. A. 2008, *ApJ*, 677, 105
- Vink, J., & Laming, J. M. 2003, *ApJ*, 584, 758
- Völk, H. J., Berezhko, E. G., & Ksenofontov, L. T. 2005, *A&A*, 433, 229
- Warren, J. S., et al. 2005, *ApJ*, 634, 376
- Wilms, J., Allen, A., & McCray, R. 2000, *ApJ*, 542, 914
- Winkler, P. F., & Long, K. S. 1997, *ApJ*, 491, 829
- Winkler, P. F., Gupta, G., & Long, K. S. 2003, *ApJ*, 585, 324
- Winkler, P. F., Long, K. S., Hamilton, A. J. S., & Fesen, R. A. 2005, *ApJ*, 624, 189
- Yamaguchi, H., et al. 2008, *PASJ*, 60, S141